arXiv:1409.0355v1 [nlin.PS] 1 Sep 2014

Nonlinear propagating localized modes in a 2D hexagonal crystal lattice

J. Bajars[1,2], J. C. Eilbeck[1,3], and B. Leimkuhler[1,2]
[1]Maxwell Institute,
[2]School of Mathematics, University of Edinburgh
James Clerk Maxwell Building, The King's Buildings,
Mayfield Road, Edinburgh EH9 3JZ, UK,
[3]Department of Mathematics, Heriot-Watt University,
Riccarton, Edinburgh EH14 4AS, UK

September 2, 2014

Abstract

In this paper we consider a 2D hexagonal crystal lattice model first proposed by Marín, Eilbeck and Russell in 1998. We perform a detailed numerical study of nonlinear propagating localized modes, that is, propagating discrete breathers and kinks. The original model is extended to allow for arbitrary atomic interactions, and to allow atoms to travel out of the unit cell. A new on-site potential is considered with a periodic smooth function with hexagonal symmetry. We are able to confirm the existence of long-lived propagating discrete breathers. Our simulations show that, as they evolve, breathers appear to localize in frequency space, i.e. the energy moves from sidebands to a main frequency band. Our numerical findings contribute to the open question of whether exact moving breather solutions exist in 2D hexagonal layers in physical crystal lattices.

1 Introduction

This article examines propagating nonlinear localized modes in crystalline materials. These modes are commonly referred to as propagating discrete breathers, i.e. waves contained within a bell-shaped envelope exhibiting internal oscillations of frequencies outside the phonon band. There is strong interest in such breather solutions, as they provide possible mechanisms underpinning physical phenomena, for example the formation of long decorated dark lines in muscovite mica [3, 20, 21, 22, 25], a possible mechanism for high temperature superconductivity [23, 19], and the development of next generation plasma fusion reactors [24]. Laboratory and numerical experiments provide evidence for such coherent localized phenomena [26, 24, 28, 8, 17, 19, 18, 13].

The existence of dark lines in muscovite mica crystals was first highlighted by Russell some twenty years ago [22]. Although some of these lines were thought to be formed by cosmic rays, the fact that many of the lines follow crystallographic axes was puzzling. Russell was unable to find a suitable linear theory for such phenomena and suggested the possibility of nonlinear localized modes. He called these "quodons" as they appeared to be connected to a symmetry feature of the axes which he called quasi-one-dimensionality, for which displacement of an atom along the axis direction was met by a force acting along the same line (technically this is C_2 symmetry). In this paper we use the term quasi-one-dimensional to refer both to this type of symmetry and to the fact that the observed mobile pulses seem to be highly localized along one of the crystallographic axes. The two effects are believed to be related [17], although the exact mechanism is not clear.

The active component in the mica case seems to be the 2D hexagonal layer of K atoms sandwiched between two relatively rigid silicate layers. Such a symmetry feature may be also associated with many of the materials having high T_c superconductivity properties [23], although in this case the underlying 2D layers have a higher cubic rather than hexagonal symmetry. More tenuous suggestions that localized modes could lead to enhanced fusion rates in deuterated crystals have also been put forward [24].

More generally, there is increasing interest in single 2D hexagonal crystals such as graphene [11] and other layered structures that could be built from the two-dimensional atomic crystals based on graphene geometries [12]. An open question is what role both stationary and mobile localized modes can play in such structures.

Due to advances in computer power and better understanding of molec-

ular dynamics algorithms [2, 14], we are now well equipped for numerical study of discrete breathers in higher dimensional dynamical lattices. There is a good theoretical and numerical understanding of existence of stationary discrete breathers [9, 4, 15], that is, spatially localized time-periodic excitations. The same cannot be said about mobile discrete breathers in 1D and higher dimensional dynamical lattices [9, 4, 10, 5, 16]. There are still open theoretical questions regarding the existence of propagating discrete breathers in general nonintegrable lattices. There are a few exceptions such as the Ablowitz-Ladik chain [1], which is an integrable model. Thus we must rely on numerical studies of propagating localized modes, the main focus of this paper. In addition, we propose here a 2D model with a lower level of complexity for future analytical investigations.

In their work, Marín et al. [17, 18] showed numerically for the first time the existence of propagating localized modes (discrete breathers) in a 2D dynamical hexagonal nonlinear lattice. They extended their results to a 2D cubic lattice in [19]. Their lattices were subject to a nearest neighbour anharmonic interparticle interaction potential and an on-site potential. Their model represents a 2D nonlinear lattice when embedded in a surrounding 3D lattice and as such can be thought of as a 2D layer model of a 3D layered crystal lattice. Examples of such crystals are cuprates, the copper-oxide based high temperature superconductors, with cubic symmetry, and muscovite mica, a potassium based silicate insulators, with hexagonal symmetry. The study [17] was limited by available computer power and hence only to models of 16^2 and 32^2 lattices sizes (i.e. < 1000 lattice sites) with periodic boundary conditions. This numerical study confirmed the existence of propagating highly localized quasi-one-dimensional discrete breathers propagating in crystallographic directions. The quasi-one-dimensional nature of the discrete breathers suggests that they may exist in crystals containing any 1D chains with C_2 symmetry.

The present paper explores the hexagonal model in much greater detail, using a much larger computational domain to simulate a system of up to 3×10^5 lattice sites. Using somewhat smaller 2D domains but with periodic boundary conditions, we are able to track a breather traversing one million lattice sites. Our study shows frequency sharpening effects in both 1D and 2D, which were not observed in the paper of Marin et al. [17]. Moreover, we obtain a better understanding of the 2D qualitative nature of these quasi-one-dimensional propagating breathers.

For the theory stated above to be a proper representation of physical real-

ity, discrete breathers must travel long distances, i.e. one or more millimeters, if we are to associate them with the creation of dark lines in mica and to give numerical support for sputtering experiment carried out by Russell et al. [24]. In this experiment, a specimen of muscovite mica of size $\sim$ 1mm. in thickness and $\sim$7mm. across the (001)-face was subject to low energy alpha particle bombardment at one end of the crystal. The experiment showed that particles were emitted at the opposite face of the specimen in the crystallographic directions of the potassium layer of muscovite. The potassium layer is thought to be the layer where discrete breathers could have propagated [25]. In general discrete breathers are not *a priori* expected to be long-lived since the lattice models considered are likely to be nonintegrable. In addition, their lifespan is subject to interactions with defects and with the phonon background, which may be viewed as thermal noise. The experiment by Russell et al. [24] showed the transport of energy over more than 10^7 lattice sites at about 300°K (room temperature). An obvious challenge is to demonstrate the existence of long-lived propagating discrete breather solutions using a theoretical model to understand their role in the transport of energy in sputtering experiments and formation of the dark lines in mica.

The simulations of Marín et al. [17] were done on small lattices with periodic boundary conditions: the longest distance of breather travel was reported to be $\leq 10^4$ lattice sites (i.e. traversing the periodic lattice many times) before the wave collapsed. Their results suggest that the discrete breathers are sensitive to small scale interactions with phonon background, i.e. thermal noise may turn propagating modes into stationary ones, or scatter their energy into the lattice, and thus lifetimes were insufficient to support the experimental results of Russell et al [24]. On the other hand this does not preclude the existence of long-lived propagating breather solutions when the right conditions are met, since the study by Cretegny et al. [7] showed that phonons may turn stationary breathers into a mobile one. The paper [17] used a lattice configuration in its dynamical equilibrium state for the initial conditions, while additionally exciting three atoms in one of the crystallographic direction with positive-negative-positive or vice versa initial velocity conditions. With these initial conditions they were able to create a propagating breather solution together with low amplitude phonons which spread into the domain and continued to interact with the propagating breather. Thus these interactions could be responsible for the collapse of propagating discrete breather.

The model in [17] was highly restricted in that it incorporated only nearest

neighbour interactions between potassium atoms, with the atoms confined to their unit cells. Thus they were not able to study kink solutions in a 2D hexagonal lattice. The objective of this paper is to eliminate this constraint, to allow short and long range interactions between potassium atoms and perform a conceptual numerical study of long-lived breather solutions. The current approach also allows us to study kink solutions in a 2D hexagonal lattice.

The paper is organised in the following way. In Section 2 we consider in detail the theoretical model we use in our study. We derive a dimensionless set of equations in Sec. 3, and in Sec. 4 we investigate the linearised system and derive the linearised dispersion relation. In Sec. 5 we report on a number of numerical simulations of long-lived breathers in our model system. Section 6 is devoted to a brief discussion of simulations of kink solutions, which do not appear to travel long distances in the present model. Some mathematical details are presented in two appendices.

2 Mathematical model

In this section we describe a 2D mathematical K-K sheet layer model of muscovite mica crystal. We model the potassium layer of mica of N potassium atoms by classical Hamiltonian dynamics with the Hamiltonian:

$$\begin{aligned} H &= K + V + U \\ &= \sum_{n=1}^{N} \left(\frac{1}{2} m \|\dot{\boldsymbol{r}}_n\|^2 + U(\boldsymbol{r}_n) + \frac{1}{2} \sum_{\substack{n'=1, \\ n' \neq n}}^{N} V(\|\boldsymbol{r}_n - \boldsymbol{r}_{n'}\|) \right), \end{aligned} \tag{1}$$

where K is the kinetic energy, U is the on-site potential energy encompassing forces from the silicate layers of atoms above and below the potassium K-K sheet, and V is the radial interaction potential between the potassium atoms. In the Hamiltonian (1), $\boldsymbol{r}_n \in \mathbf{R}^2$ is the 2D position vector of the n^{th} potassium atom with mass m, and $\dot{\boldsymbol{r}}_n$ is its time derivative. The symbol $\|\boldsymbol{u}\|$ refers to the Euclidean two-norm of a vector $\boldsymbol{u}$, i.e. its length.

2.1 Forces between crystal layers

The potassium K-K sheet of muscovite mica crystal is compactly sandwiched between rigid layers of silicon-oxygen tetrahedra which enforces hexagonal

lattice symmetry on potassium atoms [22]. Marín et al. [17] considered the rigid silicon-oxygen layer approximation and anharmonic interaction Morse forces between free potassium and fixed oxygen atoms to obtain an on-site force as a superposition of these forces for each site. In this paper we adopt a simpler approach and consider a periodic smooth on-site potential with hexagonal symmetry from [29]. This can be thought of as a generalization of a discrete 1D sine-Gordon lattice to a two dimensions with hexagonal symmetry. The on-site potential function resembles an egg-box carton and can be written as

$$\begin{aligned} U(x,y) =& \frac{2}{3}U_0\Bigg(1-\frac{1}{3}\Bigg(\cos\left(\frac{4\pi y}{\sqrt{3}\sigma}\right) \\ &+\cos\left(\frac{2\pi(\sqrt{3}x-y)}{\sqrt{3}\sigma}\right)+\cos\left(\frac{2\pi(\sqrt{3}x+y)}{\sqrt{3}\sigma}\right)\Bigg)\Bigg), \end{aligned} \tag{2}$$

where σ is the lattice constant, i.e. the equilibrium distance between potassium atoms, and $U_0 > 0$ is the maximal value of the on-site potential. Note that a simple product of cosine functions would not provide the required hexagonal symmetry. In Figure 1(a), we plot the on-site potential function (2) with sixteen sites, $\sigma = 1$ and $U_0 = 1$. In Figure 1(b) we show potassium atoms in their dynamical equilibrium states together with their labels in (x, y) coordinates. We will adopt these labels and notation in Secs. 4 and 5.

For further reference and analysis we write down the harmonic approximation to an on-site potential well

$$U_h(x,y) = \frac{16\pi^2 U_0}{18\sigma^2}\Bigg((x-x_0)^2+(y-y_0)^2\Bigg), \tag{3}$$

where (x_0, y_0) are any local minima, equilibrium states, of the on-site potential (2), see Fig. 1.

For small atomic displacements, each potassium atom K will remain in each particular site. This was imposed as a global constraint in [17] with nearest neighbour interactions. In our approach we can allow atoms to move from one site to another. In addition, the on-site potential (2) provides a simpler implementation, since function (2) is periodic and defined on all of $\mathbf{R}^2$. In the 1D approximation, i.e. y =constant, this on-site potential (2) reduces to the cosine function which is the on-site potential of the discrete sine-Gordon equation and a periodic potential of the 1D model considered

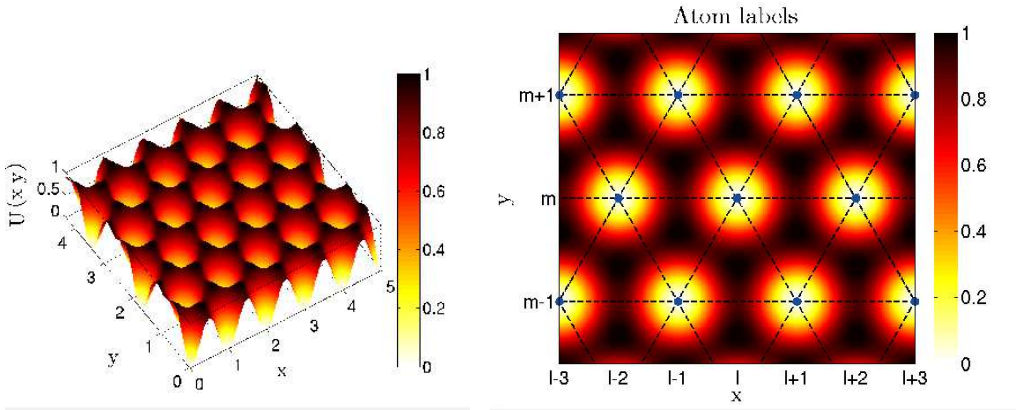

(a) (b)

Figure 1: Smooth periodic on-site potential function with hexagonal symmetry in (x, y) coordinates. (a) on-site potential with sixteen sites, $\sigma = 1$ and $U_0 = 1$. (b) configuration of potassium atoms in dynamical equilibrium states with discrete labels (l, m) in (x, y) coordinates.

in [8]. The model in [8] could be thought as a 1D approximation of the 2D model (1). To see that, without loss of generality, consider $y = 0$ in the equation (2) which leads to the cosine function in the 1D approximation. The same holds true for other two crystallographic lattice directions. The hexagonal lattice, as demonstrated in Fig. 1(b), has three crystallographic lattice directions which can be prescribed by the direction cosine vectors: $(1, 0)^T$ and $(1/2, \pm\sqrt{3}/2)^T$.

2.2 Nonlinear interaction forces

In this section we describe an empirical interaction potential to model the atomic interactions of potassium atoms in the K-K sheet of mica. Essentially, from a modelling point of view, we are concerned with anharmonic radial interaction potentials $V(r) = V(\epsilon, \sigma, r)$ parametrized by $\epsilon > 0$, the depth of the potential well, i.e. $V(\epsilon, \sigma, \sigma) = -\epsilon$, and $\sigma > 0$, the equilibrium distance, i.e. $\partial_r V(\epsilon, \sigma, \sigma) = 0$. In addition, we require that $\partial_{rr} V(\epsilon, \sigma, \sigma) > 0$ and $V(\epsilon, \sigma, r)$ are monotonically increasing functions for $r < \sigma$ and $r > \sigma$ such that

$$\lim_{r\to\infty} V(\epsilon, \sigma, r) = 0, \quad \lim_{r\to\infty} \partial_r V(\epsilon, \sigma, r) = 0. \tag{4}$$

As a first step to understanding the properties of the crystalline solids in this model, it is natural to consider the short-ranged scaled Lennard-Jones interaction potential

$$V_{LJ}(r) = \epsilon \left(\left(\frac{\sigma}{r} \right)^{12} - 2 \left(\frac{\sigma}{r} \right)^{6} \right), \tag{5}$$

where σ coincide with the lattice constant in the on-site potential (2), $r := r_{n,n'} = ||\boldsymbol{r}_n - \boldsymbol{r}_{n'}||$ for all $n, n' = 1, \ldots, N$ and $n \neq n'$. Recall that the term r^{-6} describes long range attractive van der Waals force and the term r^{-12} models Pauli short range repulsive forces. Other possible models are the Morse potential and the Buckingham potential, among others.

The Lennard-Jones potential (5) has the asymptotic properties (4). To increase the efficiency of the numerical computations, and to provide a suitable model for nearest neighbour interactions, we introduce an additional parameter in the potential (5), that is, a cut-off radius r_c. In this paper we are concerned with a close range interaction model, i.e. $r_c = \sqrt{3}\sigma$, which resembles but is not restricted to the fixed nearest neighbour interaction model.

We compared our numerical results to longer ranged interaction simulations, that is, with $r_c = 2\sigma$ and $r_c = 3\sigma$, and did not observe any qualitative differences in our results. We attribute this to the asymptotic properties (4) of the Lennard-Jones potential (5).

To incorporate the cut-off radius, we set potential and forces to zero for all atomic distances larger than r_c. For smooth cut-off computations we proceed in a similar manner as presented in [27]. Instead of only two polynomial terms, we add five additional even order polynomial terms to the interaction potential $V(r)$, i.e.

$$V_{cut}(r) = \begin{cases} V(r) + \epsilon \displaystyle\sum_{j=0}^{4} A_j \left(\frac{r}{r_c} \right)^{2j}, & 0 < r \leq r_c, \\ 0, & \text{otherwise}, \end{cases} \tag{6}$$

where the cut-off dimensionless coefficients $A_j \to 0$ when $r_c \to \infty$ and are determined from the following five conditions:

$$\begin{gathered} V_{cut}(\sigma) = V(\sigma), \quad \partial_r V_{cut}(\sigma) = \partial_r V(\sigma), \quad \partial_{rr} V_{cut}(\sigma) = \partial_{rr} V(\sigma), \\ V_{cut}(r_c) = 0, \quad \partial_r V_{cut}(r_c) = 0. \end{gathered} \tag{7}$$

In the definition of the cut-off potential (6), we only consider even power polynomial terms of the atomic radius r such that we do not need to compute square roots of atomic distances in the simulations. The particular choice of conditions (7) implies that the harmonic approximation of the cut-off potential (6) is equal to the harmonic potential approximation of $V(r)$:

$$V_h(r) = -\epsilon + 36\epsilon \left(\frac{r}{\sigma} - 1\right)^2.$$

Thus the linear analysis of the system for the nearest neighbour interactions with potential $V_{cut}(r)$ is equivalent to the linear analysis of the system with the original potential $V(r)$.

In A, we give exact formulas for the cut-off coefficients A_j of an arbitrary potential $V(r)$ satisfying the following properties: $V \to 0$ and $r\partial_r V \to 0$ when $r \to \infty$. The Lennard-Jones potential (5) satisfies these two properties. In Figure 2(a) we compare the Lennard-Jones potential (5) with the Lennard-Jones potential with cut-off radius $r_c = \sqrt{3}\sigma$ computed by (6). Due to the construction, the potential well is very well preserved despite the additional polynomial terms in the potential. With Figure 2(b) we confirm that the cut-off coefficients A_j tend to zero when the cut-off radius r_c tends to infinity. Thus in the limit we recover the original Lennard-Jones potential (5).

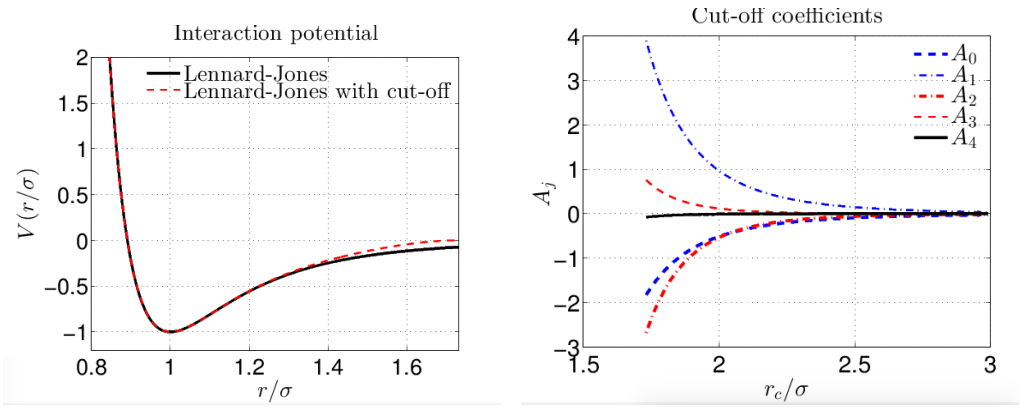

(a) (b)

Figure 2: Radial interaction potential $V(r)$. (a) Lennard-Jones potential compared to the Lennard-Jones potential with cut-off radius $r_c = \sqrt{3}\sigma$. (b) cut-off coefficients for the Lennard-Jones potential as functions of the cut-off radius r_c/σ.

3 Dimensionless system of equations

In this section we derive a dimensionless system of equations. We consider the Hamiltonian (1) with the on-site potential (2) and the interaction potential (6), that is, a system with total energy

$$H = \sum_{n=1}^{N} \Bigg(\frac{1}{2} m ||\dot{\boldsymbol{r}}_n||^2 + U(U_0, \sigma, \boldsymbol{r}_n) + \frac{1}{2} \sum_{n'=1,\, n' \neq n}^{N} \Bigg(V(\epsilon, \sigma, r_{n,n'}) + \epsilon \sum_{j=0}^{4} A_j \left(\frac{r_{n,n'}}{r_c} \right)^{2j} \Bigg) \Bigg),$$

where $r_{n,n'} = ||\boldsymbol{r}_n - \boldsymbol{r}_{n'}||$ and the potentials are represented with their set of parameters and variables. We introduce a characteristic length scale σ and time scale T of the system, i.e. $\boldsymbol{r}_n = \sigma \bar{\boldsymbol{r}}_n$ and $t = T\bar{t}$. Thus $r_{n,n'} = \sigma \bar{r}_{n,n'}$, $r_c = \sigma \bar{r}_c$, $\dot{\boldsymbol{r}}_n = \sigma/T \dot{\bar{\boldsymbol{r}}}_n$ and $H = m\sigma^2/T^2 \bar{H}$, where $\bar{H}$ is the dimensionless Hamiltonian function. Choosing the time scale $T = \sigma\sqrt{m/U_0}$ such that $H = U_0 \bar{H}$, the dimensionless Hamiltonian $\bar{H}$ of the dimensionless variables is

$$\bar{H} = \sum_{n=1}^{N} \Bigg(\frac{1}{2} ||\dot{\bar{\boldsymbol{r}}}_n||^2 + U\left(1, 1, \bar{\boldsymbol{r}}_n\right) + \frac{1}{2} \sum_{n'=1,\, n' \neq n}^{N} \Bigg(V\left(\bar{\epsilon}, 1, \bar{r}_{n,n'}\right) + \bar{\epsilon} \sum_{j=0}^{4} A_j \left(\frac{\bar{r}_{n,n'}}{\bar{r}_c} \right)^{2j} \Bigg) \Bigg),$$

where $\bar{\epsilon} = \epsilon/U_0$ is a dimensionless parameter, the interaction potential well depth parameter divided by the depth of the on-site potential. Dropping the bars over the variables, except for the parameter $\bar{\epsilon}$, the dimensionless dynamical system of equations is

$$\begin{aligned} \dot{\boldsymbol{r}}_n &= \boldsymbol{u}_n, \\ \dot{\boldsymbol{u}}_n &= -\partial_{\boldsymbol{r}_n} U\left(1, 1, \boldsymbol{r}_n\right) - \frac{1}{2} \partial_{\boldsymbol{r}_n} \sum_{n'=1,\, n' \neq n}^{N} \Bigg(V\left(\bar{\epsilon}, 1, r_{n,n'}\right) + \bar{\epsilon} \sum_{j=0}^{4} A_j \left(\frac{r_{n,n'}}{r_c} \right)^{2j} \Bigg), \end{aligned} \tag{8}$$

for all $n = 1, \ldots, N$, where $\boldsymbol{u}_n = \dot{\boldsymbol{r}}_n$ is the momentum. In the following we consider the dimensionless system (8) in our analysis and computations.

The dimensionless system of equations (8) contains two dimensionless parameters $\bar{\epsilon}$ and r_c, and cut-off coefficients A_j which depend on cut-off radius r_c. Independently from the value of r_c, when $\bar{\epsilon} = 0$ there is no interaction forces between potassium atoms and the system (8) decouples into a system of nonlinear oscillators. When the value of $\bar{\epsilon}$ tends to infinity, interaction forces dominate over the forces from the on-site potential, and in this case the equations describe a Lennard-Jones fluid. To find a suitable range for parameter $\bar{\epsilon}$ values such that both potentials have relatively equal strength, we compute and compare unrelaxed potentials seen by a potassium atom moving in any of the three lattice directions. In other words we fix all neighbouring atoms of a particular K atom and compute potential energies for small atomic displacements of the atom in any of three lattice directions, see Fig. 3.

In Figure 3 we show results for five parameter $\bar{\epsilon}$ values. It is evident that for $\bar{\epsilon} > 1$, the interaction forces dominate the on-site forces, and for $\bar{\epsilon} < 0.001$ the interaction forces are too small compared to the on-site forces and are negligible. Assuming atomic relative displacements from equilibrium in the range of 0.2, these results suggest that for system (8) to model the K-K sheet of muscovite mica we should choose $\bar{\epsilon} \in [1; 0.001]$. We find Fig. 3 to be in a good agreement with the numerical results. We do not observe propagating discrete breather solutions outside of this range of $\bar{\epsilon}$ values. Without loss of generality we choose $\bar{\epsilon} = 0.05$ as the main value for our numerical studies.

4 Linearised equations and dispersion relation

In this section we derive a nearest neighbour elastic spring interaction model of (8) and its dispersion relation. Recall that the cut-off coefficients A_j are chosen such that $\partial_{rr} V_{cut}(\sigma) = \partial_{rr} V(\sigma)$, see conditions (7). We consider the atom $\boldsymbol{r}_n$ with labels $n = (l, m)$, see Fig. 1(b), and its six neighbouring atoms with labels $(l \pm 1, m)$, $(l + 1, m \pm 1)$ and $(l - 1, m \pm 1)$. The force acting on atom n from atom n' is given by a vector

$$\boldsymbol{F}_{n,n'} = -\frac{1}{r} \partial_r V(r) \left(\boldsymbol{r}_n - \boldsymbol{r}_{n'} \right), \tag{9}$$

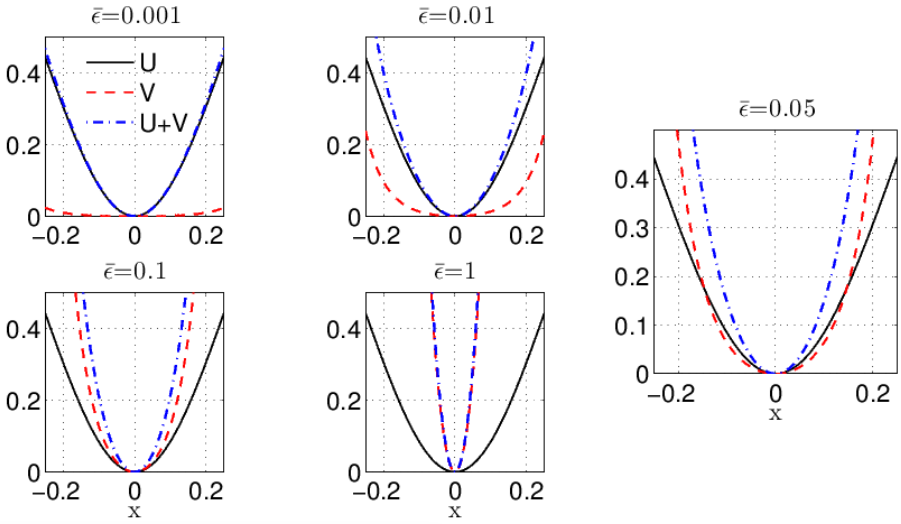

Figure 3: Unrelaxed potential dependent on dimensionless parameter $\bar{\epsilon}$ as seen by a K atom moving in any of three lattice directions, illustrated in $(x, 0)$ coordinates, $r_c = \sqrt{3}$. The solid line shows the on-site potential U, the dashed line shows the Lennard-Jones interaction potential V normalized to positive values, and the dashed dotted line shows the sum of both potentials $U + V$.

where $r \equiv r_{n,n'} = ||\boldsymbol{r}_n - \boldsymbol{r}_{n'}||$. The linearised version of (9) around the dynamical equilibrium states $\boldsymbol{r}_n^0$ and $\boldsymbol{r}_{n'}^0$ with $r^0 = ||\boldsymbol{r}_n^0 - \boldsymbol{r}_{n'}^0||$ is

$$\boldsymbol{F}_{n,n'}^{lin} = \partial_{\boldsymbol{r}_n} \boldsymbol{F}_{n,n'} \left(\boldsymbol{r}_n - \boldsymbol{r}_n^0\right) + \partial_{\boldsymbol{r}_{n'}} \boldsymbol{F}_{n,n'} \left(\boldsymbol{r}_{n'} - \boldsymbol{r}_{n'}^0\right),$$

where $\partial_{\boldsymbol{r}_{n'}} \boldsymbol{F}_{n,n'} = -\partial_{\boldsymbol{r}_n} \boldsymbol{F}_{n,n'}$, and

$$\begin{aligned} \partial_{\boldsymbol{r}_n} \boldsymbol{F}_{n,n'} &= -\partial_{rr} V\left(r^0\right) \frac{\boldsymbol{r}_n^0 - \boldsymbol{r}_{n'}^0}{r^0} \left(\frac{\boldsymbol{r}_n^0 - \boldsymbol{r}_{n'}^0}{r^0}\right)^T \\ &= -\partial_{rr} V\left(r^0\right) D_{n,n'} = -V_{r^0}'' D_{n,n'}. \end{aligned}$$

The vector $\left(\boldsymbol{r}_n^0 - \boldsymbol{r}_{n'}^0\right)/r^0$ is the corresponding direction cosine vector for the atomic pair (n, n') equilibrium positions, six in this case, and the symmetric matrix $D_{n,n'} \in \mathbf{R}^{2\times 2}$ is an outer product of the direction cosine vector.

Note that $V_{r^0}'' = 72\bar{\epsilon}$ and $r^0 = 1$ are constant when only nearest neighbour Lennard-Jones interactions are considered and recall that the harmonic approximation of the on-site potential (2) is given by (3). By dropping index

$n = (l, m)$ from matrix $D_{n,n'}$ and replacing index n' with the six neighbouring labels of atoms with labels (l, m) from Fig. 1(b), we obtain a system of dynamical linear equations

$$\begin{aligned}\ddot{\boldsymbol{w}}_{l,m} = &-\left(D_{l+2,m} + D_{l-2,m} + D_{l+1,m+1}\right.\\ &\left.+D_{l+1,m-1} + D_{l-1,m+1} + D_{l-1,m-1}\right)\boldsymbol{w}_{l,m}\\ &+ D_{l+2,m}\boldsymbol{w}_{l+2,m} + D_{l+1,m+1}\boldsymbol{w}_{l+1,m+1} + D_{l-1,m+1}\boldsymbol{w}_{l-1,m+1}\\ &+ D_{l-2,m}\boldsymbol{w}_{l-2,m} + D_{l+1,m-1}\boldsymbol{w}_{l+1,m-1} + D_{l-1,m-1}\boldsymbol{w}_{l-1,m-1}\\ &- \kappa\boldsymbol{w}_{l,m},\end{aligned} \tag{10}$$

where $\boldsymbol{w}_{l,m} = \boldsymbol{r}_{l,m} - \boldsymbol{r}^0_{l,m}$ is the displacement vector from the equilibrium state of atom (l, m) and $\kappa = 16\pi^2/9/V''_{r^0}$ after time rescaling $t = \hat{t}\sqrt{V''_{r^0}}$. In B we give exact expressions for matrices $D_{l,m}$ and system (10) in componentwise form, which are in exact agreement with the linearised equations of the Morse hexagonal lattice with an on-site harmonic potential presented in [13].

We argue here that the equation (10) with linear interaction forces together with the egg-box on-site potential (2), instead of a harmonic on-site potential (3) is a 2D model with lower level of complexity and could be used as a starting point for analytical investigations. In particular, it may be possible to develop an existence proof for propagating localized modes in this model. The proposed model can be thought as a natural extension of the discrete sine-Gordon equation in two dimensions with hexagonal symmetry. Similarly a square lattice could be considered.

Following the approach of [13], we derive a dispersion relation from the simple wave solutions

$$\boldsymbol{w}_{l,m} = \boldsymbol{A}e^{i\left(\frac{1}{2}k_1 l + \frac{\sqrt{3}}{2}k_2 m - \hat{\omega}\hat{t}\right)}, \tag{11}$$

where $\boldsymbol{A} \in \mathbf{R}^2$ is an amplitude, $\boldsymbol{k} = (k_1, k_2)$ is the wave number, and $\hat{\omega}$ is a frequency in the $\hat{t}$ time scale. Explicit calculations give the linear system matrix for $\boldsymbol{w}_{l,m}$ in (10)

$$\begin{aligned}&D_{l+2,m} + D_{l-2,m} + D_{l+1,m+1}\\ &\quad + D_{l+1,m-1} + D_{l-1,m+1} + D_{l-1,m-1} = \begin{pmatrix}3 & 0\\ 0 & 3\end{pmatrix},\end{aligned} \tag{12}$$

see B. Thus, substituting (11) and (12) into the linear system (10), we obtain

$$\begin{aligned}\mathbf{0} = &\left(\hat{\omega}^2 - \kappa - 3\right)\boldsymbol{A} + D_{l+2,m}\boldsymbol{A}e^{+ik_1} + D_{l-2,m}\boldsymbol{A}e^{-ik_1} \\ &+ D_{l+1,m+1}\boldsymbol{A}e^{i\left(\frac{1}{2}k_1+\frac{\sqrt{3}}{2}k_2\right)} + D_{l+1,m-1}\boldsymbol{A}e^{i\left(\frac{1}{2}k_1-\frac{\sqrt{3}}{2}k_2\right)} \\ &+ D_{l-1,m+1}\boldsymbol{A}e^{i\left(-\frac{1}{2}k_1+\frac{\sqrt{3}}{2}k_2\right)} + D_{l-1,m-1}\boldsymbol{A}e^{i\left(-\frac{1}{2}k_1-\frac{\sqrt{3}}{2}k_2\right)}.\end{aligned} \tag{13}$$

From the symmetry properties of matrices $D_{l,m}$, equation (13) can be simplified to

$$\begin{aligned}\mathbf{0} = &\left(\hat{\omega}^2 - \kappa - 3\right)\boldsymbol{A} \\ &+ 2\cos\left(k_1\right)\begin{pmatrix}1 & 0\\ 0 & 0\end{pmatrix}\boldsymbol{A} + \cos\left(\tfrac{1}{2}k_1\right)\cos\left(\tfrac{\sqrt{3}}{2}k_2\right)\begin{pmatrix}1 & 0\\ 0 & 3\end{pmatrix}\boldsymbol{A} \\ &- \sin\left(\tfrac{1}{2}k_1\right)\sin\left(\tfrac{\sqrt{3}}{2}k_2\right)\begin{pmatrix}0 & \sqrt{3}\\ \sqrt{3} & 0\end{pmatrix}\boldsymbol{A}\end{aligned}$$

and this leads to the dispersion relation

$$\begin{aligned}&\left(\hat{\omega}^2 - \kappa - 3 + 2\cos\left(k_1\right) + \cos\left(\tfrac{1}{2}k_1\right)\cos\left(\tfrac{\sqrt{3}}{2}k_2\right)\right) \\ &\quad\times\left(\hat{\omega}^2 - \kappa - 3 + 3\cos\left(\tfrac{1}{2}k_1\right)\cos\left(\tfrac{\sqrt{3}}{2}k_2\right)\right) \\ &\quad -3\sin^2\left(\tfrac{1}{2}k_1\right)\sin^2\left(\tfrac{\sqrt{3}}{2}k_2\right) = 0,\end{aligned} \tag{14}$$

which is in the exact agreement with the dispersion relation obtained for the Morse hexagonal lattice in [13].

The frequency solution of (14) has two positive branches for a given wavenumber $\boldsymbol{k} = (k_1, k_2)$. From (13), by setting $\boldsymbol{k} = (2\pi, 0)$, for example, we can derive the maximal frequency of the linear system (10) in $\hat{t}$ and t time scales, that is

$$\hat{\omega}_{max} = \sqrt{6+\kappa}, \quad \omega_{max} = \sqrt{6V_{r^0}'' + \frac{16\pi^2}{9}}, \quad \omega = \sqrt{V_{r^0}''}\hat{\omega},$$

respectively. In Figure 4(a) we show surface plots of frequency $\omega/2\pi$ versus wavenumber for $\bar{\epsilon} = 0.05$. In Figure 4(b), we plot normalized dispersion curves for equal components of wavenumber, that is, $k_1 = k_2$, for different values of $\bar{\epsilon}$. The normalized frequency can be expressed as

$$\frac{\omega}{\omega_{max}} = \frac{\hat{\omega}}{\hat{\omega}_{max}} = \frac{\sqrt{\alpha(k_1,k_2) + \kappa(\bar{\epsilon})}}{\sqrt{6+\kappa(\bar{\epsilon})}}$$

which tends to unity when $\bar{\epsilon} \to 0$ for each value of $(k_1, k_2) \in \mathbf{R}^2$. Hence $\omega \to \omega_{max} = 4\pi/3$ when $\bar{\epsilon} \to 0$, the case of a decoupled system of harmonic oscillators of potential energy (3) with $U_0 = 1$.

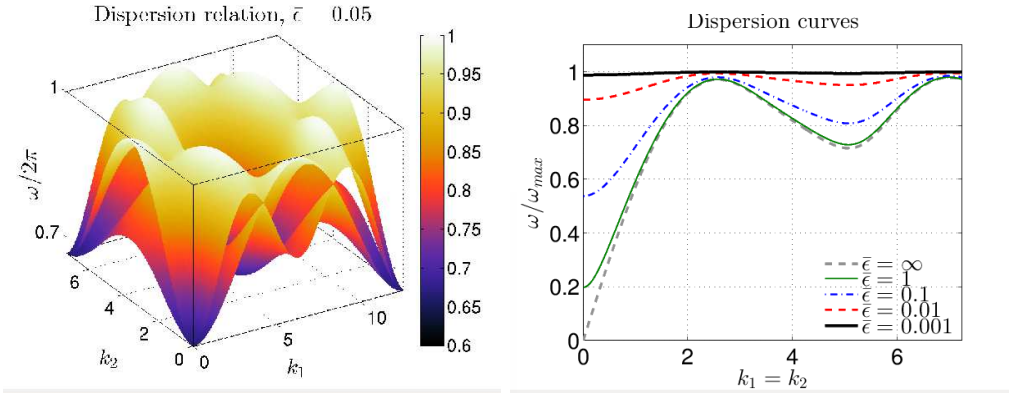

(a) (b)

Figure 4: Dispersion relation of the linearised 2D hexagonal crystal lattice equations. (a) two branches of positive frequency $\omega/2\pi$, $\bar{\epsilon} = 0.05$. (b) normalized upper branch dispersion curves for equal components of the wavenumber, i.e. $k_1 = k_2$, and different values of $\bar{\epsilon}$.

5 Numerical simulations of propagating discrete breathers

In this section we describe numerical simulations of propagating discrete breathers obtained by solving the initial value problem (8). We integrate the Hamiltonian dynamics (8) in time with a second order time reversible symplectic Verlet method [2, 14]. In the following, all numerical examples are performed with $\bar{\epsilon} = 0.05$, $r_c = \sqrt{3}$, time step $\tau = 0.04$ and periodic boundary conditions. To excite mobile discrete breathers, we consider the lattice in its dynamical equilibrium state, see Fig. 1(b), and excite three neighbouring atomic momenta with the pattern

$$\boldsymbol{v}_0 = \gamma(-1; 2; -1)^T, \tag{15}$$

where the values of $\gamma \neq 0$ depend on the choice of $\bar{\epsilon}$. Single kicks or different patterns of simultaneous kicks can be considered as well as the excitation

given above. Our objective is to consider initial conditions which produce the least amount of phonon background which may interfere with the study of propagating discrete breathers. This particular choice of pattern (15) gave the cleanest initial conditions for the computations of propagating discrete breathers. The following results are presented with $\gamma = 0.5$.

The main observed properties of propagating discrete breathers were qualitatively similar for different values of the cut-off radius r_c, for $\bar{\epsilon}$ values when propagating discrete breathers can be observed, time steps τ, for different initial momenta patterns and for different values of γ. However, long time numerical simulations are sensitive to initial conditions, small changes in parameter and time step values as well as to round-off errors. This is due to the chaotic nature of the underlying dynamical system.

To display the energy over the lattice, we define an energy density function by assigning to each atom its kinetic energy and on-site potential values as well as half of the interaction potential values. Since the energy H may take also negative values, and to explore better small scales of the system for plotting purposes only, we replace the total energy of the system by

$$H_{log} = \log(H + |\min\{H\}| + 1)$$

such that $H_{log} \geq 0$.

As a first example, we consider a periodic rectangular lattice: $N_x = 100$ and $N_y = 16$, where N_x and N_y are the number of atoms in x and y axis directions, respectively. We place the initial momentum pattern (15) in the middle of the domain with respect to the y axis. We integrate the system in time up to 1000 time units. In Fig. 5 we demonstrate the evolution of the energy density function in time. For plotting purposes we have interpolated the energy density function on a rectangular mesh. The peaks of energy in Fig. 5 are associated with the propagating discrete breather. To perform this test, we also included a damping of the atomic momenta at the upper and lower boundaries for the initial time interval $t \in [0; 100]$, to reduce the amount of phonons which spread over the domain. The propagating breather moves to the right on the horizontal line, i.e. on the horizontal crystallographic lattice line, and is highly localized in space. Evidently, from Fig. 5, the initial pattern (15) with a small amount of initial damping at the boundaries for some time interval, has created a clean breather solution with small amplitude phonon background not visible to the naked eye.

In Figure 6 we plot atomic displacements from their equilibrium states in the x and y axis directions at the final computational time, i.e. $T_{end} = 1000$.

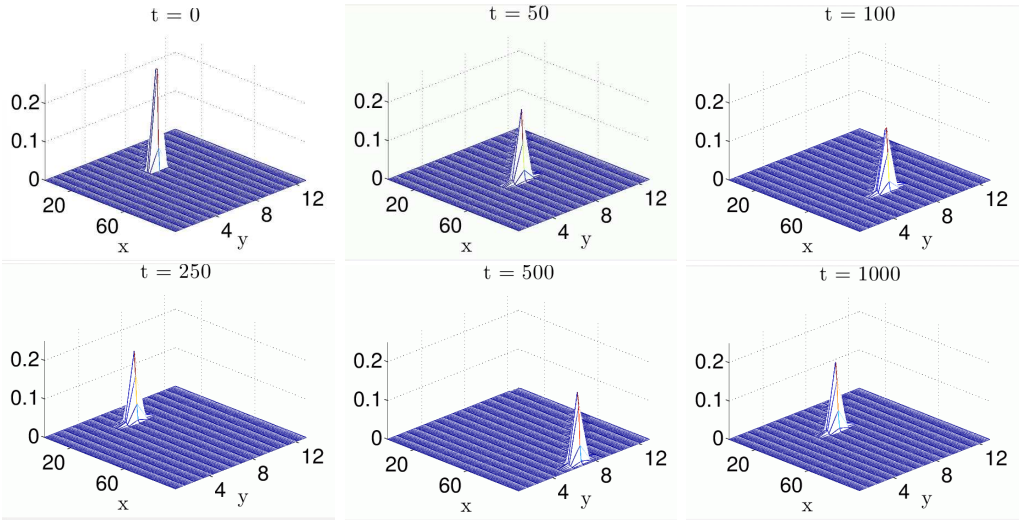

Figure 5: Evolution of the energy density function in time and energy localization around the propagating discrete breather solution.

We indicate the displacement function in the x axis direction by Δx and in the y axis direction by Δy. Comparing Figures 6(a) and 6(b), we notice the differences in the scales of the displacements. From Figure 6(a), it is evident that the largest displacement in the x direction is on the main chain of atoms along which the breather propagates and there are only very small amplitude displacements in adjacent chains. From Figure 6(b), it can be seen that on the main chain there is almost zero displacement in the y direction, whilst there is visible displacement of the adjacent chains. Notice the anti-symmetry between breather displacements on adjacent chains in Fig. 6(b).

To understand better the localization properties of the propagating breather solutions, we compute the maximal and minimal displacement values in atomic chains where the breather has propagated over a specified computational time interval. We assign the index m to the horizontal main chain of atoms along which the breather has propagated, and indices $m \pm k$ where $k = 1, 2, 3$ to the adjacent chains of atoms, see Fig. 1(b). We refer to these chains by y_m. The displacement plot of maximal and minimal values is shown in Fig. 7(a). The figure confirms that the largest displacement of atoms is on the main chain y_m in the x direction with almost zero displacement in y axis direction. Figure 7(a) is in good agreement with Figs. 6(a) and 6(b). Notice that there is still some displacement in both axis directions for atoms

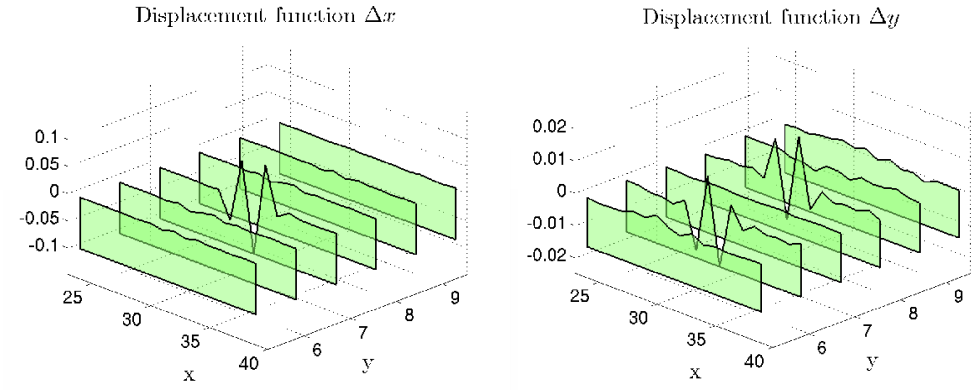

(a) (b)

Figure 6: Atomic displacements in space from their equilibrium states at final computational time $T_{end} = 1000$. (a) displacement function Δx in the x axis direction. (b) displacement function Δy in the y axis direction.

in adjacent chains $y_{m\pm3}$. This is due to the presence of phonons in the lattice. Compared to the breather energy, the phonon energy is very small, as can be seen in Fig. 7(b), where we plot the maximal energy of atoms over time.

Evidently, most of the energy is localized on the atoms on the main chain y_m and rapidly decays along the y axis directions. Thus in the y axis direction the breather is localized on around five atoms while at the same time it is localized on around seven to eight atoms in the x axis direction, see Fig. 6(a). Closer inspection of Figs. 7(a) and 7(b) shows that maximal and minimal displacements in the x axis directions, as well as the energy, is symmetric with respect to the adjacent chains $y_{m\pm k}$ where $k = 1, 2, 3$, while maximal and minimal displacements in the y axis directions are anti-symmetric. This is because when the breather propagates on the main chain y_m, it pushes atoms *away* on adjacent chains. The maximum displacement away from the main chain is larger compared to the maximum displacement towards the main chain y_m.

The displacement values in Fig. 7(a) are dependent on the values of $\bar{\epsilon}$ and γ. For larger values of γ, we observed larger displacement values in the x axis directions of the atoms on the main chain y_m. The same is true for smaller values of $\bar{\epsilon}$. Interestingly, smaller values of $\bar{\epsilon}$ gave smaller values of displacements in the y direction on adjacent chains, and hence increases the quasi-one-dimensional nature of propagating discrete breathers.

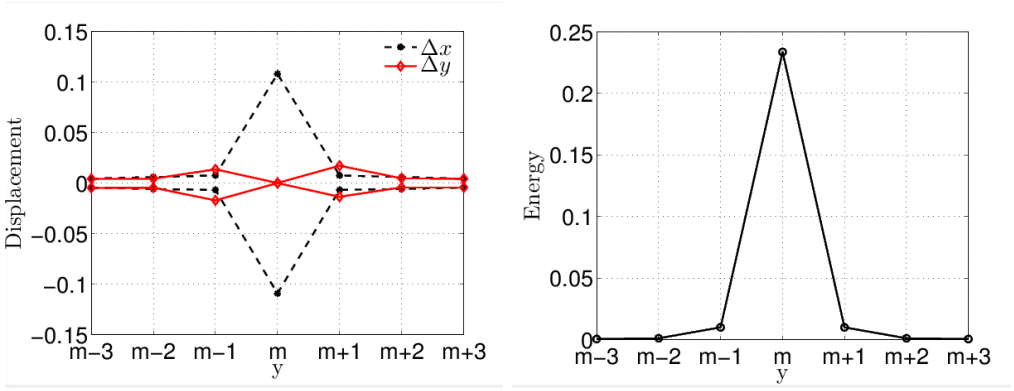

(a) (b)

Figure 7: Spacial displacements and energy of the propagating discrete breather. (a) maximal and minimal displacements in x and y axis directions on atomic chains over computational time interval. (b) maximal energy in chains of atoms over computational time interval.

Indeed, Figure 7(b) indicates the quasi-one-dimensional nature of propagating discrete breathers. Despite the small amount of energy in adjacent chains of atoms, the energy is still strongly localized. That can be seen in Fig. 8. In Figure 8(a), we plot the energy density function of the chain y_m at each time unit. Similarly we plot the energy density functions as a function of time in the adjacent chains y_{m+1} and y_{m+2}, see Figs. 8(b) and 8(c), respectively. As before, for plotting purposes we interpolated the results on the uniform mesh.

We pick maximal colour scales according to the values in Fig. 7(b). The amount of the breather energy in the chain y_m is much higher as compared to the phonon energies; none of these energies are visible in Fig. 8(a). On the contrary, the small amount of phonon energy is visible in Figs. 8(b) and 8(c), thus confirming the presence of phonon waves in the lattice. The damping initiated in the simulation at initial times at the boundaries does not remove the phonons completely from the system, and these phonons will affect the long term solution of the propagating discrete breather in the lattice with periodic boundary conditions. Questions regarding the energy loss by the breather solution, its velocity, focusing properties and lifespan will be addressed in the following sections.

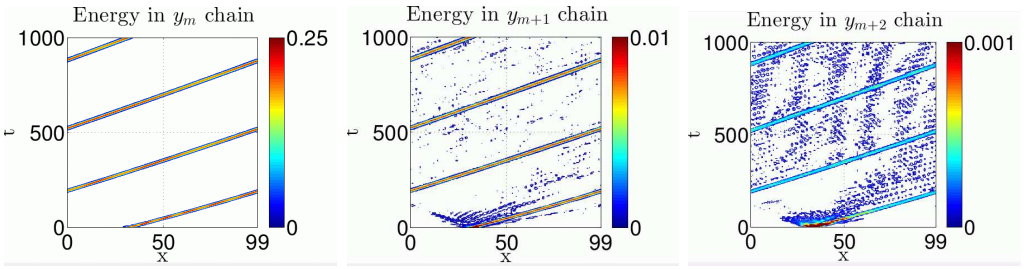

(a) (b) (c)

Figure 8: Contour plots of the breather energy on atomic chains in time. (a) breather energy on the main chain y_m. (b) breather energy on the adjacent chain y_{m+1}. (c) breather energy on the adjacent chain y_{m+2} (note different colour scales).

5.1 Focusing of discrete breathers in frequency space

In the previous section, we described how to excite propagating discrete breathers and discussed the energy localization properties in atomic chains of the propagating discrete breather. In this section we study a novel feature, the focusing property in the frequency domain, that is, the spectral properties of 2D propagating discrete breather solutions. For our study we consider numerical simulations on the rectangular long strip lattice: $N_x = 20000$ and $N_y = 16$, with periodic boundary conditions. We integrate in time until the breather has reached the right hand end of the lattice, that is, after around 10^5 time units in our example. For this example we kept damping at the upper and lower boundary until the breather has passed 500 sites, to remove some amount of the phonons from the lattice, thus obtaining cleaner data. We collected time series data of the displacement function $\Delta x_m(t)$ at 100 equally spaced atoms on the main chain along which the breather propagates. From the data obtained, we compute the spectrum and plot the squared amplitude of the discrete Fourier transform in Fig. 9(a). We illustrate the same result but in the squared amplitude versus frequency domain in Fig. 9(b), where we plot each tenth section of Fig. 9(a).

Two main observations can be drawn from Fig. 9. The first is that the breather frequency is above the phonon frequency band, compare Fig. 9(a) to Fig. 4(a). The second observation is that the propagating breather is focusing in frequency space as it evolves. As a result, we observe spreading of the breather in the time domain, which is illustrated in Fig. 10. In Figure 10,

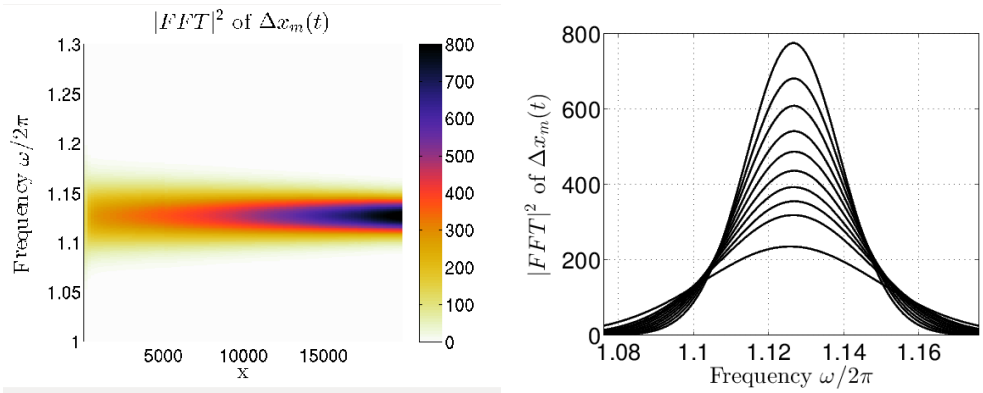

(a) (b)

Figure 9: Propagating breather frequency spectrum. (a) amplitude squared of the time series of displacement function $\Delta x_m(t)$ on the main lattice chain y_m. (b) ten cross-sections of plot (a).

we show the time series of the displacement function $\Delta x_m(t)$ on a normalized time axis of three atoms from the main chain y_m. Notice that the amplitude of the breather in Fig. 10 does not change, only the width of the wave. Importantly, we observed such focusing effects also in 1D versions of our 2D lattice model. This naturally raises the question whether the spreading of the breather occurs also in the spatial domain. In our numerical results, we did not observe such phenomenon. It would be interesting to see if such frequency sharpening, as breathers evolve, also arises in other 1D and 2D models.

In our long strip lattice simulations we were not able to reach saturation in frequency space, we need simulations over longer lattice strips and for longer times. See the results of Sec. 5.3, where we have performed long time simulation of propagating breather solution on a 200×16 lattice with periodic boundary conditions. Notice the relative saturation in the frequency space, despite the presence of phonons.

The spreading of the breather in the time domain suggests that the breather is slowing down, since it takes longer to pass through one atom in space. We confirm this by computing the breather velocity in time, see Fig. 11(a). The graph is obtained by tracking the location of the breather in space. From this data we compute the breather velocity. The smoothed out normalized curve of breather velocity is shown in Fig. 11(a). At the same

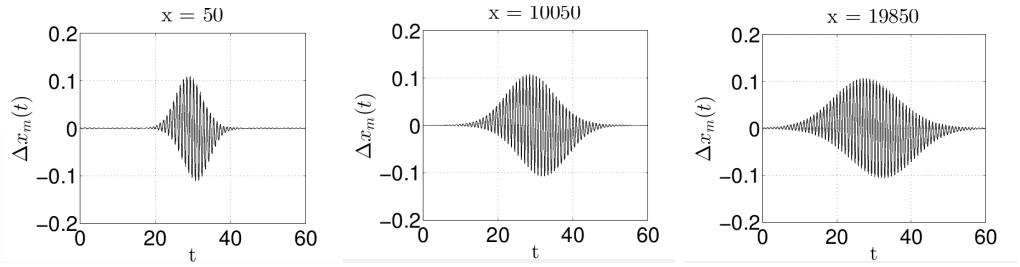

Figure 10: Spreading of the propagating breather solution in time, as demonstrated by the displacement function $\Delta x_m(t)$ at three locations in the spacial domain on the chain y_m. Computational times are normalized to the same time axis.

time, we compute the breather energy in time, which is estimated from the sum of energies over multiple atoms. A smoothed out normalized curve of the breather energy is illustrated in Fig. 11(b). Figure 11 shows that the propagating breather is slowing down and loosing its energy. Our numerical tests showed that there is a strong correlation between breather velocity and focusing in the frequency space. The breather focuses when it slows down and defocuses when it speeds up. In some rare cases we could observe time intervals of constant breather velocity with no focusing or defocusing in frequency space. In the next section we show that the same focusing effect is occurring in adjacent chains.

5.2 Focusing in adjacent chains

In this section we demonstrate the focusing properties of the propagating breather in adjacent chains of atoms. We consider the same numerical example above and collect time series data of displacement functions $\Delta x_{m+1}(t)$, $\Delta y_{m+1}(t)$, $\Delta x_{m+2}(t)$ and $\Delta y_{m+2}(t)$ of equally spaced atoms in lattice. Recall that the breather propagates on the lattice chain y_m. For the atom displacement functions on adjacent lines, we produce equivalent figures to Fig. 9(a), see Fig. 12. The dashed line indicates the dominant frequency of the Fig. 9(a). All plots of Fig. 12 show the same focusing effect, but with smaller amplitudes as indicated by the colour bars.

It is interesting that Figs. 12(b) and 12(c) show focusing towards the same dominant frequency of the displacement function $\Delta x_m(t)$ while the displacement functions $\Delta x_{m+1}(t)$ and $\Delta y_{m+2}(t)$ appear to be focusing on two

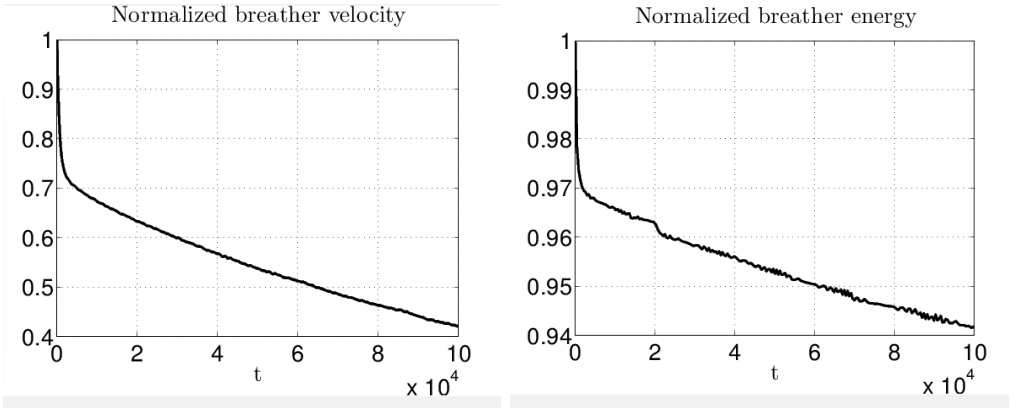

(a) (b)

Figure 11: Long strip lattice simulation, (a) normalized breather velocity in time, (b) normalized breather energy in time.

frequencies above the phonon band, see Figs. 12(a) and 12(d), respectively. This split of frequencies can be attributed to modulation by the rotational frequencies. That can be seen in Fig. 13, where we plot phase portraits of the displacement functions of one atom in the middle of the computational domain over the time interval when the breather passes through. In other words, Fig. 13 shows 2D breather displacements of atoms in lattice chains adjacent to the main lattice chain y_m. In Figure 13(a), we illustrate the phase portrait of the functions $\Delta x_{m+1}(t)$ and $\Delta y_{m+1}(t)$, and in Fig. 13(b) we illustrate the phase portrait of the functions $\Delta x_{m+2}(t)$ and $\Delta y_{m+2}(t)$. Notice the rotational character of the 2D propagating discrete breather in the adjacent lattice chains y_{m+1} and y_{m+2}.

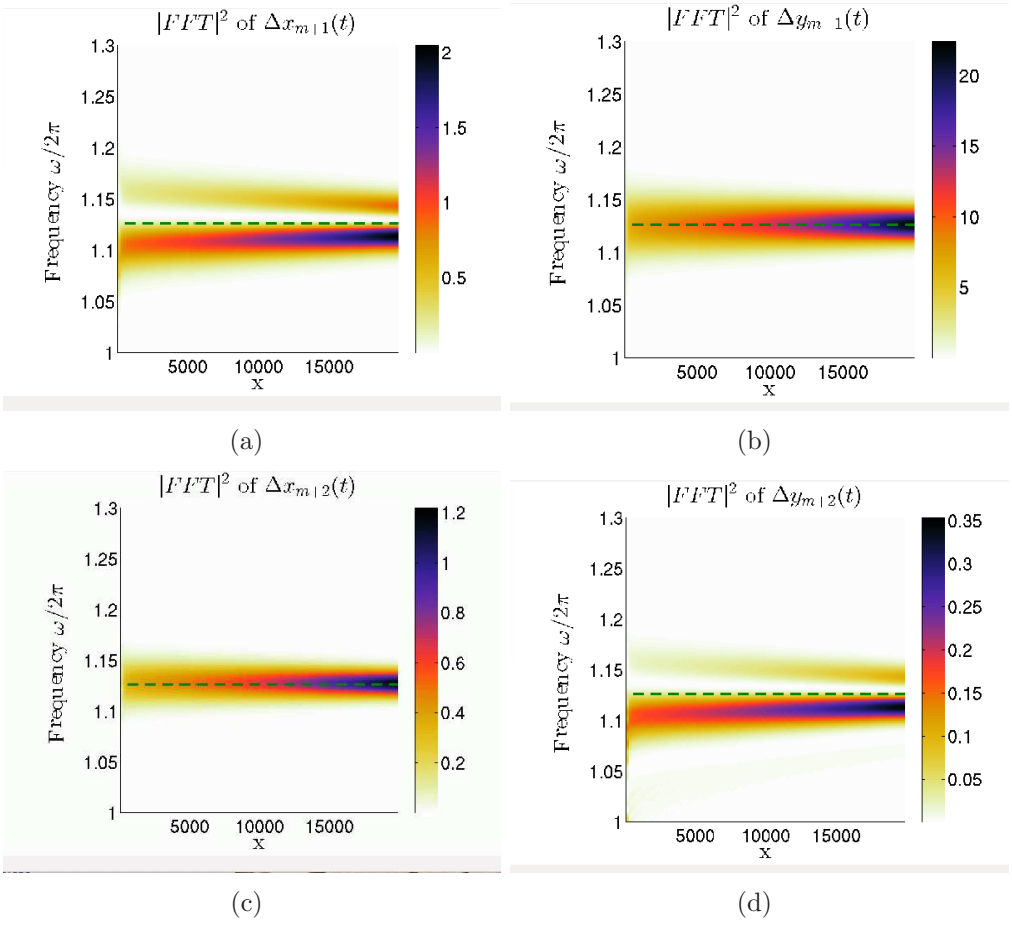

Figure 12: Frequency spectrum of a propagating breather in adjacent chains ($m+1$ and $m+2$). (a) amplitude squared of the time series of the displacement function $\Delta x_{m+1}(t)$ on the lattice chain y_{m+1}. (b) amplitude squared of the time series of the displacement function $\Delta y_{m+1}(t)$ on the lattice chain y_{m+1}. (c) amplitude squared of the time series of the displacement function $\Delta x_{m+2}(t)$ on the lattice chain y_{m+2}. (d) amplitude squared of the time series of the displacement function $\Delta y_{m+2}(t)$ on the lattice chain y_{m+2}.

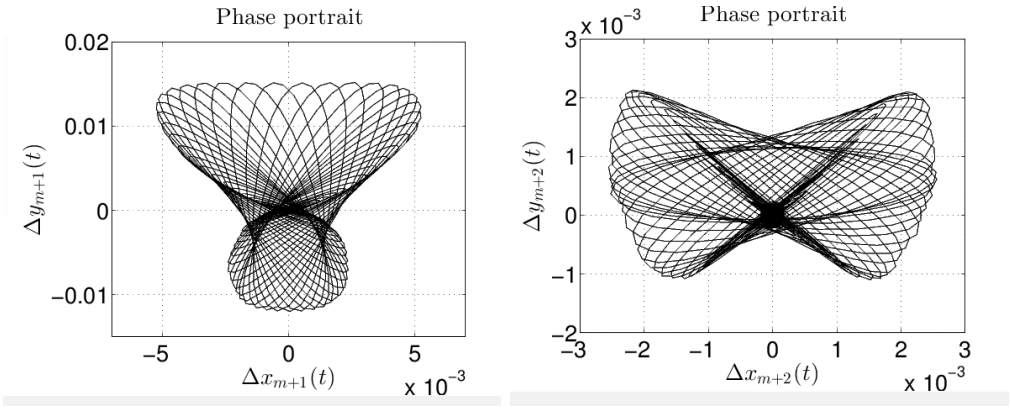

(a) (b)

Figure 13: 2D displacements of atoms in lattice chains y_{m+1} and y_{m+2} over the time when breather has passed through. (a) phase portrait of $\Delta x_{m+1}(t)$ and $\Delta y_{m+1}(t)$. (b) phase portrait of $\Delta x_{m+2}(t)$ and $\Delta y_{m+2}(t)$.

5.3 Long-lived breather solutions

In the sections above, we performed numerical simulations of propagating discrete breathers and discussed their properties, in particular, the localization of energy and focusing in frequency space. It is still an open question if exact propagating discrete breathers exist in our model. Figure 11 shows that the propagating breather slows down and loses its energy. Long time studies of propagating discrete breathers are subject to the chaotic nature of molecular dynamics model, round-off errors and interactions with the phonon background. All these aspects lead to the unpredictable nature of results and sensitive dependence on initial conditions. Thus analytical studies are needed to answer the question regarding existence of propagating discrete breathers. At the same time this serves as a good motivation to study breather interactions with phonons, i.e. breather propagation in thermalized crystals, and interactions between breathers themselves, which we report elsewhere.

To contribute to the discussion of the existence of the breather solutions, we perform a conceptual numerical study of breather lifespan in a periodic lattice. We consider a lattice: $N_x = 200$ and $N_y = 16$, with periodic boundary conditions. We excite a breather solution with atomic momenta pattern (15), $\gamma = 0.5$, in the $(1, 0)^T$ crystallographic lattice direction on a chain y_m.

This initial condition is integrated in time until the breather has passed one million lattice sites, i.e. crossed the computational domain 5000 times. In our example, that took less than 10^7 time units. As before, we kept damping at the upper and lower boundaries, in this case until the breather has passed 2000 sites.

In Figure 14(a), we plot the number of sites the breather has passed versus time. The normalized breather velocity is plotted in time in Figure 14(b), computed from the curve in Fig. 14(a). In addition, after each 50 breather propagation cycles, we collected the time series of displacement function $\Delta x_m(t)$ of an atom at the middle of the computational domain on the lattice chain y_m. The computed frequency spectrum of time series is illustrated in Fig. 14(c), where the x axis of the figure refers to the number of sites the breather has passed in Fig. 14(a). Figures 14(b) and 14(c) show the relative saturation in breather velocity and frequency spectrum over time. Small scale variations are attributed to the presence of the weak phonon background.

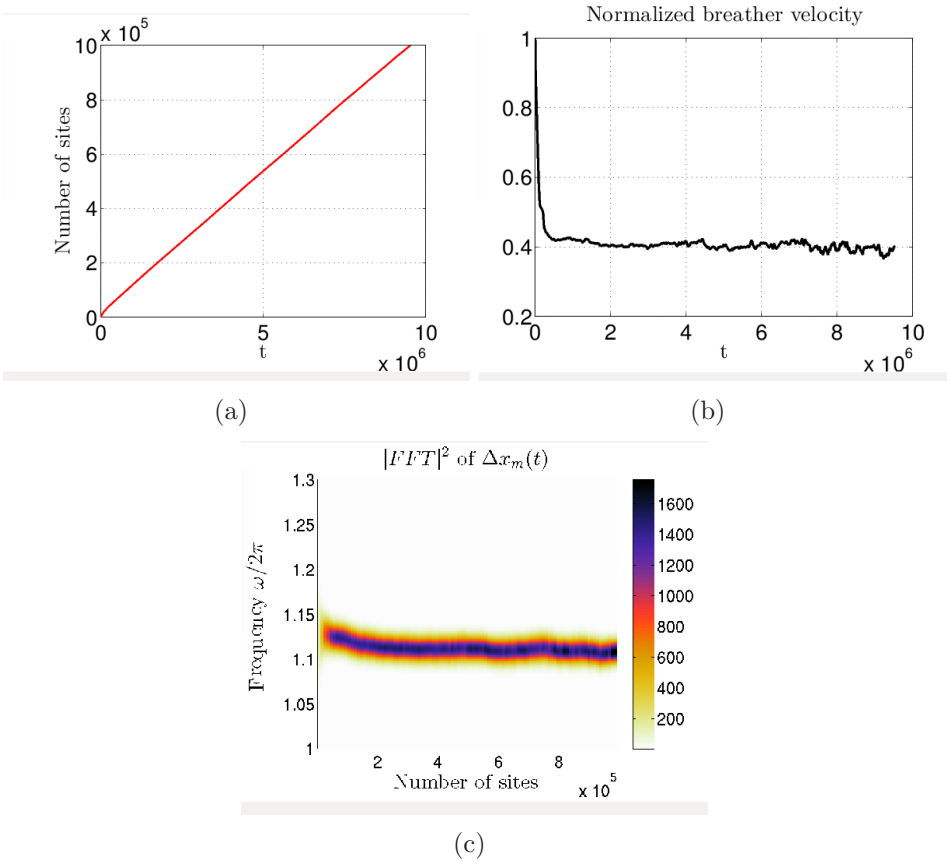

Figure 14: Long-lived breather simulation, $N_x = 200$ and $N_y = 16$. (a) number of sites the breather has passed versus time. (b) normalized breather velocity in time. (c) breather frequency spectrum of the displacement function $\Delta x_m(t)$ on the y_m chain.

The numerical results in Figure 14 demonstrates long-lived mobile breather solution in a weakly thermalized background by phonons. The breather solution has propagated over one million lattice sites, i.e. more than a factor $100\times$ of that reported by Marín et al. [17]. It would be interesting to establish a relation between the breather's lifespan and the lattice temperature for different values of $\bar{\epsilon}$.

6 Kink solutions

In this section we briefly discuss kink solutions. Recall that our model allows atoms to be displaced outside unit cells, in comparison to the model by Marín et al. [17]. To excite kink solutions, we consider one atom momentum initial kicks $\boldsymbol{v}_0 = \gamma$ in $(1, 0)^T$ in a crystallographic lattice direction on the lattice chain y_m. We were not able to excite kink solutions with parameter $\bar{\epsilon} = 0.05$ and $\tau = 0.04$ values. By reducing the parameter values of $\bar{\epsilon}$ and τ we were able to observe a highly localized short-lived kink propagating initially along the atomic chain y_m.

In Figure 15, we show the position of the kink, as estimated by the position of the maximal energy density, as it evolves. It starts at the hollow circle on the left, and initially travels in a straight line along a crystallographic lattice direction. We suppress plots of other lower energy excitations created by the kick, such as breathers, phonons, etc. The kink radiates energy through phonons and eventually switches to a more random route, eventually coming to a halt at the position marked by a filled circle on the right. For topological reasons the kink cannot be destroyed unless it collides with an anti-kink.

We have performed numerical tests with different values of initial kicks $\boldsymbol{v}_0$, $\bar{\epsilon}$, r_{cut} and time step τ, and did not observe solutions which persisted along a single direction, in contrast to [6], where the same egg-box carton on-site potential (2) was considered, but used a piecewise polynomial interaction potential instead of the Lennard-Jones (5). In this latter paper with this different potential, we did observe long-lived kink solutions. These findings suggest that the choice of interaction potential and its relative strength with respect to the on-site potential may play a significant role in the stability of kink solutions. It remains to be seen if existing or novel 2D materials can exhibit such kinks in physical situations.

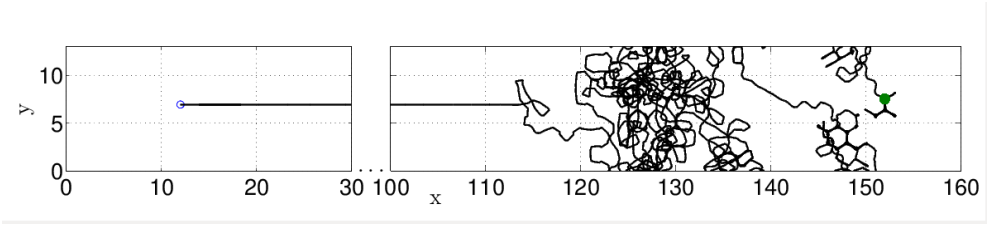

Figure 15: Kink solution, position trace of the maximal energy density function. $N_x = 160$, $N_y = 16$, $T_{end} = 10^4$, $r_{cut} = \sqrt{3}$, $\bar{\epsilon} = 0.01$, $\boldsymbol{v}_0 = 4$ and $\tau = 0.01$.

7 Summary

In this article, we provide a detailed qualitative study of propagation breather solutions, building on and expanding the work of of Marín et al. [17] and performed a qualitative study of propagating breather solutions. By considering a periodic smooth "egg-box carton" on-site potential, and a scaled Lennard-Jones interaction potential with a cut-off radius, we have derived a dimensionless system of equations with one dimensionless parameter $\bar{\epsilon}$. This parameter is the ratio of the depth of the interaction potential to that of the on-site potential. We have found a range of parameter $\bar{\epsilon}$ values with which mobile breathers can be observed. This parameter range was found to be in a good agreement with numerical observations and the considerations of [17] that both potentials should be of equal relative strength.

The Lennard-Jones interaction potential with cut-off was constructed such that harmonic approximation agrees with the harmonic approximation of the Lennard-Jones potential itself. With this in mind, we derived the nearest neighbour linearised equations of phonons. The derivation of the linearised equations and its dispersion relation allow us to confirm that breather internal frequency spectrum is above the phonon band. Thus, together with numerical observations, we were able to confirm that the propagating localized modes are optical breather solutions. In addition, we argue that the linear nearest neighbour interaction model, together with egg-box on-site potential could be a suitable model of lower level of complexity for analytical investigations. Such an argument follows from a natural analogy with the 1D discrete sine-Gordon equation.

In the study of propagating breather solutions, we confirmed its quasi-one-dimensional nature as well as its 2D characteristics. We showed that the

most of the breather energy is localized on the main chain of atoms along which the breather propagates, and that it propagates in crystallographic lattice directions. In addition, we showed that there is also a strong localization of energy present in adjacent chains of atoms. From the time series of atomic displacements in both the x and y axis directions, we were able to demonstrate the 2D rotational character of the atomic motion in adjacent chains over the time interval when breather passes through. From the same time series data, we computed the frequency spectrum and presented the novel finding of breather localisation in frequency space as it evolves. This behaviour causes the breather to spread in time, while preserving its amplitude. We found a correlation between the localization in frequency space and the breather's velocity. We found the same localization property in adjacent chains of atoms. It would be very interesting to see if other 1D or 2D models with breather solutions support the same localization property in frequency space as the breather evolves.

To reach the saturation regime where the frequency sharpening stabilises would take a very long time with long strip lattice simulations, a computationally challenging task. In addition, the chaotic nature of the molecular dynamics system, together with the existent phonon background added by the initial condition, give further challenges to long time simulations. We chose to add a small amount of damping for short initial time interval to reduce the phonon density in the system.

To contribute to the open question of whether propagating breather solutions exist, we performed conceptual long time simulation on a *small* lattice with periodic boundary conditions. Despite the presence of the phonon background, we were able to observe a long-lived breather solution travelling over one million lattice sites, a factor of 100 more than previous results. This numerical experiment showed a relative saturation in the breather's velocity, that is, an almost constant velocity with small variations, and a relative saturation in the frequency spectrum. The fluctuations in the velocity and spectral results are due to the presence of the weak phonon background. Importantly, this numerical result serves as a good motivation for a study of breather interactions and propagation in thermalized lattices, hinting to the possibility of long-lived breather solutions in more realistic physical situations.

We concluded our findings with a brief discussion of kink solutions. Our model allows the displacements of atoms out of the unit cell, in comparison to the model by Marín et al. [17]. We found no kink solutions travelling long

distances, in contrast to the findings in [6], where long-lived kink solutions were observed in a 2D hexagonal crystal lattice with a different inter-particle potential. It is clear that kink solutions are strongly affected by the choice of interaction potentials, and it remains to be shown if materials exist which can exhibit such kinks in physical situations.

Acknowledgements

JB and BJL acknowledge the support of the Engineering and Physical Sciences Research Council which has funded this work as part of the Numerical Algorithms and Intelligent Software Centre under Grant EP/G036136/1.

A Cut-off coefficients

In this Appendix we derive a linear system of equations and its solution to find the cut-off coefficients A_j for the interaction potential (6). The cut-off coefficients are determined from the conditions (7) which form a linear system of equations:

$$\begin{gathered}\sum_{j=0}^{4}\frac{\sigma^{2j}}{r_c^{2j}}A_j=0,\quad \sum_{j=1}^{4}\frac{2j\sigma^{2j-1}}{r_c^{2j}}A_j=0,\quad \sum_{j=1}^{4}\frac{2j(2j-1)\sigma^{2j-2}}{r_c^{2j}}A_j=0,\\ \sum_{j=0}^{4}A_j=-\tilde{V},\quad \sum_{j=0}^{4}2jA_j=-r_c\tilde{V}_r,\end{gathered}\tag{16}$$

where $\tilde{V}=V(r_c)/\epsilon$ and $\tilde{V}_r=\partial_r V(r_c)/\epsilon$. In addition we require that $\tilde{V}\to 0$ and $r_c\tilde{V}_r\to 0$ when $r_c\to\infty$.

The system of equations (16) can be solved analytically to give

$$
\begin{aligned}
A_0 &= \frac{1}{2}\frac{\left(r_c\sigma^2 - r_c^3\right)\tilde{V}_r + \left(8r_c^2 - 2\sigma^2\right)\tilde{V}}{\left(r_c^2-\sigma^2\right)^4}\sigma^6,\\
A_1 &= -\frac{1}{2}\frac{\left(2r_c^2\sigma^2 + \sigma^4 - 3r_c^4\right)\tilde{V}_r + 24r_c^3\tilde{V}}{\left(r_c^2-\sigma^2\right)^4}r_c\sigma^4,\\
A_2 &= \frac{3}{2}\frac{\left(\sigma^4 - \ r_c^4\right)\tilde{V}_r + \left(8r_c^3 + 4r_c\sigma^2\right)\tilde{V}}{\left(r_c^2-\sigma^2\right)^4}r_c^3\sigma^2,\\
A_3 &= -\frac{1}{2}\frac{\left(3\sigma^4 - 2r_c^2\sigma^2 - r_c^4\right)\tilde{V}_r + \left(8r_c^3 + 16r_c\sigma^2\right)\tilde{V}}{\left(r_c^2-\sigma^2\right)^4}r_c^5,\\
A_4 &= \frac{1}{2}\frac{\left(\sigma^2 - r_c^2\right)\tilde{V}_r + 6r_c\tilde{V}}{\left(r_c^2-\sigma^2\right)^4}r_c^7.
\end{aligned}
$$

The coefficients A_j are shown in non-dimensionless form. To obtain them in dimensionless form, we set $\sigma = 1$ and use dimensionalized functions $\tilde{V}$ and $\tilde{V}_r$.

B Linear system and outer products of direction cosines

In this appendix, we give explicit expressions for the direction cosine vectors, their outer products and the linear system (10) in component-wise form. The atom (l, m) has six neighbouring atoms $(l+2, m)$, $(l-2, m)$, $(l+1, m+1)$, $(l+1, m-1)$, $(l-1, m+1)$ and $(l-1, m-1)$, and associated direction cosines $(1, 0)^T$, $(-1, 0)^T$, $(1/2, \sqrt{3}/2)^T$, $(1/2, -\sqrt{3}/2)^T$, $(-1/2, \sqrt{3}/2)^T$ and $(-1/2, -\sqrt{3}/2)^T$. Thus the six outer products of the direction cosines are

$$
D_{l\pm2,m} = \begin{pmatrix} 1 & 0 \\ 0 & 0 \end{pmatrix}, \quad D_{l+1,m\pm1} = \begin{pmatrix} \frac{1}{4} & \pm\frac{\sqrt{3}}{4} \\ \pm\frac{\sqrt{3}}{4} & \frac{3}{4} \end{pmatrix}, \quad D_{l-1,m\pm1} = \begin{pmatrix} \frac{1}{4} & \mp\frac{\sqrt{3}}{4} \\ \mp\frac{\sqrt{3}}{4} & \frac{3}{4} \end{pmatrix}.
$$

Applying these matrices to (10), we derive linear equations in component-wise form:

$$
\begin{aligned}
\ddot{u}_{l,m} = &- 3u_{l,m} + \tfrac{1}{4}\left(u_{l+1,m+1} + u_{l+1,m-1} + u_{l-1,m+1} + u_{l-1,m-1}\right)\\
&+ \left(u_{l+2,m} + u_{l-2,m}\right)\\
&+ \tfrac{\sqrt{3}}{4}\left(v_{l+1,m+1} - v_{l+1,m-1} - v_{l-1,m+} + v_{l-1,m-1}\right) - \kappa u_{l,m},
\end{aligned}
$$

$$\ddot{v}_{l,m} = -3v_{l,m} + \frac{3}{4}\left(v_{l+1,m+1} + v_{l+1,m-1} + v_{l-1,m+1} + v_{l-1,m-1}\right) + \frac{\sqrt{3}}{4}\left(u_{l+1,m+1} - u_{l+1,m-1} - u_{l-1,m+1} + u_{l-1,m-1}\right) - \kappa v_{l,m},$$

where $\boldsymbol{w}_{l,m} = (u_{l,m}, v_{l,m})$, that is, the displacements of atom (l, m) from its equilibrium position in the x and y directions.

References

[1] M. J. Ablowitz and J. F. Ladik. Nonlinear differential-difference equations and Fourier analysis. *Journal of Mathematical Physics*, 17:1011, 1976.

[2] M. P. Allen and D. J. Tildesley. *Computer Simulation of Liquids*. Oxford science publications. Oxford University Press, USA, 1989.

[3] J. Archilla, editor. *Procceedings of Qudons in mica: nonlinear localized travelling excitations in crystals, meeting in honour of Prof. Mike Russell, Altea, September 18-21, 2013*, Springer Material Science. Springer-Verlag, in press.

[4] S. Aubry. Discrete breathers: Localization and transfer of energy in discrete Hamiltonian nonlinear systems. *Physica D: Nonlinear Phenomena*, 216(1):1–30, 2006.

[5] S. Aubry and T. Cretegny. Mobility and reactivity of discrete breathers. *Physica D: Nonlinear Phenomena*, 119(1-2):34–46, 1998.

[6] J. Bajars, J. C. Eilbeck, and B. Leimkuhler. Numerical simulations of nonlinear modes in mica: past, present and future. In J. Archilla, editor, *Quodons in Mica: nonlinear localized travelling excitations in crystals*, Springer Material Science, pages ??–?? Springer-Verlag, in press. Procceedings of the meeting "Quodons in Mica: nonlinear localized travelling excitations in crystals", in honour of Prof. Mike Russell, Altea, Spain, September 18-21, 2013. (ArXiv 1408.6853).

[7] T. Cretegny, S. Aubry, and S. Flach. 1D phonon scattering by discrete breathers. *Physica D: Nonlinear Phenomena*, 119(1-2):73–87, 1998.

[8] Q. Dou, J. Cuevas, J. C. Eilbeck, and F. M. Russell. Breathers and kinks in a simulated crystal experiment. *Discrete and Continuous Dynamical Systems - Series S*, 4:1107–1118, 2011.

[9] S. Flach and A. V. Gorbach. Discrete breathers - Advances in theory and applications. *Physics Reports*, 467(1-3):1–116, 2008.

[10] S. Flach and K. Kladko. Moving discrete breathers? *Physica D: Nonlinear Phenomena*, 127(1-2):61–72, 1999.

[11] A. K. Geim. Graphene: Status and prospects. *Science*, 324:1530–1534, 2009.

[12] A. K. Geim and I. V. Grigorieva. Van der Waals heterostructures. *Nature*, 499:419–425, 2013.

[13] K. Ikeda, Y. Doi, B. F. Feng, and T. Kawahara. Chaotic breathers of two types in a two-dimensional Morse lattice with an on-site harmonic potential. *Physica D*, 225:184–196, 2007.

[14] Benedict Leimkuhler and Sebastian Reich. *Simulating Hamiltonian Dynamics*. Cambridge University Press, 2005.

[15] R. S. MacKay and S. Aubry. Proof of existence of breathers for time-reversible or Hamiltonian networks of weakly coupled oscillators. *Nonlinearity*, 7(6):1623, 1994.

[16] R. S. MacKay and J.-A. Sepulchre. Effective Hamiltonian for travelling discrete breathers. *Journal of Physics A: Mathematical and General*, 35(18):3985, 2002.

[17] J. L. Marín, J. C. Eilbeck, and F. M. Russell. Localized moving breathers in a 2D hexagonal lattice. *Physics Letters A*, 248:225–229, 1998.

[18] J. L. Marín, J. C. Eilbeck, and F. M. Russell. 2-D Breathers and applications. In P. L. Christiansen, M. P. Søerensen, and A. C. Scott, editors, *Nonlinear Science at the Dawn of the 21th Century*, pages 293–306. Springer, Berlin, 2000.

[19] J. L. Marín, F. M. Russell, and J. C. Eilbeck. Breathers in cuprate-like lattices. *Physics Letters A*, 281:21–25, 2001.

[20] F. M. Russell. Identification and selection criteria for charged lepton tracks in mica. *International Journal of Radiation Applications and Instrumentation. Part D. Nuclear Tracks and Radiation Measurements*, 15:41–44, 1988.

[21] F. M. Russell. Decorated track recording mechanisms in muscovite mica. *International Journal of Radiation Applications and Instrumentation. Part D. Nuclear Tracks and Radiation Measurements*, 19:109–114, 1991.

[22] F. M. Russell and D. R. Collins. Lattice-solitons and non-linear phenomena in track formation. *Radiation Measurements*, 25:67–70, 1995.

[23] F. M. Russell and D. R. Collins. Anharmonic excitations in high T_c materials. *Physics Letters A*, 216:197–202, 1996.

[24] F. M. Russell and J. C. Eilbeck. Evidence for moving breathers in a layered crystal insulator at 300K. *Europhysics Letters*, 78:10004, 2007.

[25] F. M. Russell and J. C. Eilbeck. Persistent mobile lattice excitations in a crystalline insulator. *Discrete and Continuous Dynamical Systems - Series S*, 4:1267–1285, 2011.

[26] P. Sen, J. Akhtar, and F. M. Russell. MeV ion-induced movement of lattice disorder in single crystalline silicon. *Europhysics Letters*, 51:401, 2000.

[27] S. D. Stoddard and J. Ford. Numerical Experiments on the Stochastic Behavior of a Lennard-Jones Gas System. *Physical Review A*, 8(3):1504–1512, 1973.

[28] B. I. Swanson, J. A. Brozik, S. P. Love, G. F. Strouse, A. P. Shreve, A. R. Bishop, W.-Z. Wang, and M. I. Salkola. Observation of intrinsically localized modes in a discrete low-dimensional material. *Physical Review Letters*, 82:3288–3291, 1999.

[29] Y. Yang, W. S. Duan, L. Yang, J. M. Chen, and M. M. Lin. Rectification and phase locking in overdamped two-dimensional Frenkel-Kontorova model. *Europhysics Letters*, 93(1):16001, 2011.